

Diverse microstructures of magnetorheological fluid induced by shear flows (A direct numerical investigation)

Tsutomu ANDO*, Ryoga FUJII*, Osamu KOIKE**, Rei TATSUMI** and Noriyuki HIROTA***

*Department of Mechanical Engineering, College of Industrial Technology, Nihon University

1-2-1 Izumi-cho, Narashino, Chiba 275-8575, Japan

E-mail: ando.tsutomu@nihon-u.ac.jp

**Products Innovation Association

2-11-16 Yayoi, Bunkyo-ku, Tokyo 113-8656, Japan

***Optical Ceramics Group, Optical Materials Field, Research Center for Electronic and Optical Materials, National Institute for Materials Science

1-2-1 Sengen, Tsukuba, Ibaraki 305-0047, Japan

Received: 6 November 2025; Revised: 14 January 2026; Accepted: 2 March 2026

Abstract

This study presents numerical simulations of magnetorheological (MR) fluids under a wide range of shear rates using the Euler-Lagrange hybrid scheme. In a confined space between plane-parallel walls with gravity neglected, under a constant magnetic field and particle volume fraction, the formation of magnetic particle microstructures and the shear-thinning behavior of the apparent viscosity of the MR fluid are investigated. As the shear rate increases, the microstructures formed by the magnetic particles transition from chain-like to sheet-like formations around a Mason number (Mn) of 1. Beyond a certain shear threshold, these structures begin to aggregate toward the stationary wall, while particles move away from the moving wall. For $Mn = 30$, hydrodynamic two-phase separation is observed with respect to the vertical direction of the walls: a particle-free region appears on the moving wall side, while an aggregate structure without interparticle contact forms on the stationary wall side. With further increase in shear rate to $Mn = 100$, the upper-layer particles of the aggregates detach and disperse. The two-phase separation observed at $Mn = 30$ is induced by magnetic and hydrodynamic interactions, and the aggregation toward the stationary wall is attributed to the constraint of particle rotation by applied magnetic field. These findings indicate that the presence or absence of particle rotation influences the hydrodynamic lift forces acting on the particles. The ratio of the magnetic torque induced by the applied magnetic field to the hydrodynamic torque is as a key factor governing the microstructure of magnetic particles in MR fluids.

Keywords : Magnetorheological fluid, Shear flow, Microstructure of particles, Direct numerical simulation, Solid-liquid multiphase flow, Magnetic particle

1. Introduction

Magnetorheological (MR) fluids (Rabinow, 1948; Morillas and Vicente, 2020), whose viscosity changes in response to a magnetic field, are among the most well-known functional fluids. The viscosity can vary significantly, even approaching a nearly solid state. When MR fluids were first developed, they were anticipated for use in applications such as clutches (Rabinow, 1948), brakes (Li and Du, 2003; Rossa et al., 2014), and dampers (Spencer et al., 1997). For utilization in automotive brakes and structural dampers, MR fluids must exhibit long service life and resistance to harsh environments. Challenges in these applications include oxidation, sedimentation, and separation of magnetic particles (Kumar et al., 2019, Morillas and Vicente, 2020). In recent years, MR fluids have also been applied in virtual experience devices such as virtual reality (VR) systems, surgical training simulators (Tsujita et al., 2012), and immersive systems (Blake and Gurocak, 2009; Senkal and Guricak, 2010; Yang et al., 2020), with new application areas continuing to emerge. These devices typically require a relatively short service life and are primarily designed for indoor use. For practical implementation, it is also necessary to consider the time response of particles under external magnetic fields,

including alternating magnetic fields and oscillating shear flow conditions.

In functional fluids such as MR fluids, magnetic fluids, and Electrorheological (ER) fluids, particles align in response to external magnetic or electric fields. Theoretical calculations and numerical simulations have well established that these particles form chain-like structures along the direction of the applied magnetic field. Theoretical analyses of single-chain clusters in ER fluids (Martin and Anderson, 1996) are also applicable to MR fluids. MR fluids can generate greater shear stress than ER fluids, holding a unique position in engineering applications. In recent years, numerous simulation studies have reported the formation of sheet-like structures oriented perpendicular to parallel walls under certain shear rates (Han et al., 2010; Lagger et al., 2014, 2015; Ido et al., 2015, 2017; Peng and Pei, 2021; Pei et al., 2022). Several of these studies examined only particle structures under low shear flow conditions (Han et al., 2010; Ido et al., 2015, 2017), while others did not incorporate the rotational motion of particles induced by hydrodynamic torque (Lagger et al., 2014, 2015; Peng and Pei, 2021; Pei et al., 2022). One study investigated a wide range of shear flow fields but did not address the resulting particle structures (Lagger et al., 2015). Previous numerical simulation studies have faced challenges such as insufficient predictive capability of existing models in high shear regions ($Mn > 30$; Mn : Mason number), limitations in modeling particle rotation dynamics coupled with magnetic fields, and incomplete methodologies for linking particle microstructure to the macroscopic properties of MR fluids. In this study, direct numerical simulations were performed over a broader range of shear flow fields than those explored in prior research. As a result, previously unreported particle structures were identified, and a key governing factor was revealed. The details of these findings are presented in the following sections.

2. Numerical simulation model

This study conducted direct numerical simulations to investigate the microstructure formation of magnetic particles using the Euler-Lagrange hybrid scheme. The particle microstructure and the relative apparent viscosity were quantitatively analyzed with respect to the Mason number, which represents the ratio of hydrodynamic to magnetic force acting on a magnetic particle. A wide range of shear flow conditions up to $Mn = 100$ was investigated under a constant magnetic field and particle volume fraction.

The equations of motion for the particles in the solvent are based on Newton's equations of motion for translation and Euler's equations of motion for rotation.

$$m_p \frac{dV_i}{dt} = \sum_j \mathbf{F}_{ij}^c + \mathbf{F}_i^h + \sum_j \mathbf{F}_{ij}^m \quad (1)$$

$$I_p \frac{d\omega_i}{dt} = \sum_j \mathbf{T}_{ij}^c + \mathbf{T}_i^h + \sum_j \mathbf{T}_{ij}^m + \mathbf{T}_i^H \quad (2)$$

where t is time, m_p is the mass of the particle, V_i is the velocity of the i -th particle position \mathbf{r}_i , I_p is the moment of inertia of particle, ω_i is the angular velocity of particle i , \mathbf{F}^c and \mathbf{T}^c are the contact force and torque based on the standard formulation of the Discrete Element Method (DEM) (Tsuji et al., 1992; Fujita and Yamaguchi, 2008), and \mathbf{F}^h and \mathbf{T}^h are the hydrodynamic force and torque, respectively (Fujita and Yamaguchi, 2008; Ando et al., 2012; Makabe et al., 2021).

Several necessary terms related to magnetism and magnetic fields are introduced. A particle with a dipole moment interacts with a magnetic field \mathbf{H} to induce a force \mathbf{F} (Rosensweig, 1985; Chikazumi, 1997). The magnetic force \mathbf{F}_{ij}^m exerted on particle i by particle j is expressed as follows (Sato, 1995; Ando et al., 2018):

$$\begin{aligned} \mathbf{F}_{ij}^m &= -\nabla(-\mu_0 \mathbf{m}_i \cdot \mathbf{H}_{ij}) \\ &= -\frac{3\mu_0}{4\pi} \cdot \frac{1}{r_{ij}^4} \left[-(\mathbf{m}_i \cdot \mathbf{m}_j) \frac{\mathbf{r}_{ij}}{r_{ij}} + 5(\mathbf{m}_i \cdot \mathbf{r}_{ij})(\mathbf{m}_j \cdot \mathbf{r}_{ij}) \frac{\mathbf{r}_{ij}}{r_{ij}^3} - \{(\mathbf{m}_j \cdot \mathbf{r}_{ij})\mathbf{m}_i + (\mathbf{m}_i \cdot \mathbf{r}_{ij})\mathbf{m}_j\} \frac{1}{r_{ij}} \right] \end{aligned} \quad (3)$$

where \mathbf{m}_i and \mathbf{m}_j ($m = |\mathbf{m}_i| = |\mathbf{m}_j|$) are the magnetic moments of the particles i and j , $\mathbf{r}_{ij} = \mathbf{r}_i - \mathbf{r}_j$ is the vector connecting the centers of particles i and j , $r_{ij} = |\mathbf{r}_{ij}|$. \mathbf{H}_{ij} is the magnetic field that the magnetic moment \mathbf{m}_j exerts on the position of particle i . μ_0 is the space permeability. The torque \mathbf{T}_{ij}^m acting on particle i due to the magnetic interaction with particle j is

expressed as follows (Satoh, 1995; Ando et al., 2018):

$$\begin{aligned} \mathbf{T}_{ij}^m &= \mu_0 \mathbf{m}_i \times \mathbf{H}_{ij} \\ &= -\frac{\mu_0}{4\pi} \cdot \frac{1}{r_{ij}^3} \left\{ \mathbf{m}_i \times \mathbf{m}_j - \frac{3}{r_{ij}^2} (\mathbf{m}_j \cdot \mathbf{r}_{ij}) \mathbf{m}_i \times \mathbf{r}_{ij} \right\} \end{aligned} \quad (4)$$

The torque \mathbf{T}_i^H due to the externally applied magnetic field \mathbf{H}_{ex} ($H_{ex} = |\mathbf{H}_{ex}|$) is expressed by the following equation.

$$\mathbf{T}_i^H = \mu_0 \mathbf{m}_i \times \mathbf{H}_{ex} \quad (5)$$

The governing equations for fluid flow including particles are the incompressible condition and the Navier-Stokes equation (Ando et al., 2012; Makabe et al., 2021).

$$\nabla \cdot \mathbf{u} = 0 \quad (6)$$

$$\frac{\partial \mathbf{u}}{\partial t} + (\mathbf{u} \cdot \nabla) \mathbf{u} = -\frac{1}{\rho_f} \nabla p + \frac{\eta}{\rho_f} \nabla^2 \mathbf{u} + \Phi \boldsymbol{\alpha} \quad (7)$$

where \mathbf{u} is the fluid velocity on the computational lattice, ρ_f is the density of the solvent, p is the pressure, η is the viscosity of the solvent, Φ is the volume fraction of the particles on the computational lattice. This value is [0 (outside a particle), 1 (inside a particle)] considering the overlap between two particles (Fujita and Yamaguchi, 2008; Ando et al., 2012; Makabe et al., 2021). $\boldsymbol{\alpha}$ is the particle acceleration obtained using direct forcing in the Immersed-boundary method, which includes the convective and viscous terms (Fadlum et al., 2000).

$$\boldsymbol{\alpha} = \frac{\mathbf{v}^p - \mathbf{u}}{\Delta t} + (\mathbf{u} \cdot \nabla) \mathbf{u} - \frac{\eta}{\rho_f} \nabla^2 \mathbf{u} \quad (8)$$

This study solved the velocity fields by a two-step method (Kajishima et al., 2001; Nakayama and Yamamoto, 2005) under the constraint of Eq. (6), where the pressure was decomposed into two components: $p = p^* + p'$; with the intermediate pressure without particles, p^* , and the correcting pressure with particles, p' (Ando et al., 2012). \mathbf{v}^p is the velocity of particles on the computational lattice, as defined below:

$$\mathbf{v}^p = \mathbf{V} + \boldsymbol{\omega} \times \mathbf{r} \quad (9)$$

\mathbf{V} is the translational velocity of the particle, $\boldsymbol{\omega}$ is the angular velocity of the particle, and \mathbf{r} is the relative position from the particle center. The numerical simulation accurately resolved both the force and torque of particle-fluid hydrodynamic interactions, including many-body interactions, using the Immersed-boundary method. The hydrodynamic force \mathbf{F}_i^h and torque \mathbf{T}_i^h acting on the particle i are expressed as (Makabe et al., 2021)

$$\mathbf{F}_i^h = - \int \phi_i(\mathbf{r}) \rho_f \boldsymbol{\alpha}(\mathbf{r}) dV \quad (10)$$

$$\mathbf{T}_i^h = - \int \phi_i(\mathbf{r}) \{ \mathbf{r}_i(\mathbf{r}) \times \rho_f \boldsymbol{\alpha}(\mathbf{r}) \} dV \quad (11)$$

where ϕ_i is the volume fraction of the particle i , whose sum is Φ on the computational lattice. The approach was based on the SIMPLEST algorithm and adopted an upwind scheme for the convection term.

This study assumed the use of commercially available MR fluids with a particle volume fraction of 30%, considering

practical engineering applications such as MR brakes. The calculation conditions are listed in Table 1. The external magnetic field B_{ex} ($= \mu_0 H_{ex}$) was applied with a constant value. The solvent was assumed to be kerosene ($\rho_f = 8.09 \times 10^2 \text{ kg/m}^3$, $\eta = 2.42 \times 10^{-3} \text{ Pa} \cdot \text{s}$), while the particle was modeled as an iron-based sphere ($\rho_p = 7.8 \times 10^3 \text{ kg/m}^3$) with a certain magnetization of $M = 7.96 \times 10^4 \text{ A/m}$. Figure 1 indicates that the calculation domain is defined as $(x, y, z) = (10d, 10d, 20d)$, where the particle diameter is $d = 1.5 \text{ } \mu\text{m}$. A grid size of fluid computational lattice is $\Delta = d/9$ (Kajishima et al., 2001; Nakayama et al., 2008; Ando et al., 2012; Makabe et al., 2021). Boundary conditions were imposed to reflect the actual configuration of an MR fluid device, including both moving and stationary walls. No-slip conditions were applied at the plane-parallel walls, while periodic boundary conditions were applied on the other boundaries.

In this physical system under magnetic and shear fields, particle structures develop along the magnetic field direction or the shear direction, but not along the vorticity direction. Furthermore, the computational domain varies depending on the specific research focus. In this study, to focus on the particle structures developing along the magnetic field direction, periodic boundary conditions were employed. Previous studies (Ido et al., 2015, 2017) adopted a similar computational domain of $(11d, 11d, 21d)$ and discussed particle structures. Based on their findings and the present results, we conclude that the use of periodic boundary conditions is valid for characterizing particle structures. It is noted that no significant changes in particle structure were observed, even when a series of simulations was carried out in a smaller domain of $(6d, 6d, 12d)$ under the same shear conditions.

In the initial state of each simulation, particles were randomly distributed at a constant volume fraction of 30%. The study investigated a wide range of shear flow fields up to $Mn = 100$, where the shear rate is $\dot{\gamma} = u_w/20d = 2.28 \times 10^6 \text{ s}^{-1}$. This corresponds to a relative velocity between the walls of $u_w = 68.5 \text{ m/s}$, with the particle Reynolds number of $Re_p = 34.5$ (if $v^p = 0$), which falls within the expected operational range. This value is close to the maximum velocity observed in practical vehicular applications. However, since the particles comove with the solvent, the actual particle Reynolds number based on the particle-fluid relative velocity is $Re_p < 1$, indicating that the flow around the particles is laminar. Gravity was ignored, as the simulations did not consider gravitational settling of particles. For instance, the shear velocity at $Mn = 0.1$ is four orders of magnitude larger than the settling velocity. In particular, the resulting particle structures observed for $Mn \geq 30$ are flow-induced. Particles are typically sterically stabilized in a nonpolar medium with a protective polymer shell of a few nanometers in thickness to prevent aggregation of magnetic particles due to van der Waals interactions (Rosensweig, 1985). In this case, the van der Waals force outside the polymer shell rapidly decays and becomes significantly smaller than the magnetic force. Therefore, DLVO interaction was not considered in this simulation.

The Mason number, defined as the ratio of the hydrodynamic force due to shear flow to the magnetic force between the magnetic moments of particles, is given as follows (Klingenberg et al., 2007; Sherman et al., 2015):

$$Mn = \frac{\text{Hydrodynamic force}}{\text{Magnetic force}} = \frac{3\pi\eta d^2 \dot{\gamma}}{3\mu_0 m^2 / (4\pi d^4)} = 144 \frac{\eta \dot{\gamma}}{\mu_0 M^2} \quad (12)$$

The ratio of magnetic torque due to an applied field to hydrodynamic torque is defined as follows (Satoh, 1995):

$$R_H = \frac{\text{Magnetic torque due to applied field}}{\text{Hydrodynamic torque}} = \frac{\mu_0 m H}{\pi \eta d^3 \dot{\gamma}} = \frac{\mu_0 M H}{6 \eta \dot{\gamma}} \quad (13)$$

Equations (12) and (13) yield the following Eq. (14):

$$Mn \cdot R_H = 24 \frac{H}{M} \quad (14)$$

This study determined $Mn \cdot R_H = 120$ from Table 1. The microstructure of the MR fluid was examined in the region of $Mn < 120$, i.e., $R_H > 1$, where the applied magnetic field exceeded the hydrodynamic torque, and the particle rotation was assumed to be constrained.

The relative apparent viscosity η^* is calculated using the following equation (Fujita and Yamaguchi, 2008). The apparent viscosity η_a is determined by averaging the velocity gradient $(\partial u / \partial z)_{wall}$ at the walls.

$$\eta^* = \frac{\eta_a}{\eta} = \frac{1}{\dot{\gamma}} \left(\frac{\partial u}{\partial z} \right)_{wall} \quad (15)$$

where u is the fluid velocity in the x -direction. This study omits some effects of wall type on the dynamical microstructure of magnetized particles. The computational domain was bounded by featureless walls that were frictionless between solids and non-magnetic surfaces.

Table 1 Calculation conditions.

| Nomenclature | Value |
|-----------------------------------------------|-----------|
| H/M [-] | 5 |
| Applied magnetic field $B (= \mu_0 H)$ [T] | 0.5 |
| Mason number Mn [-] | 0.1 - 100 |

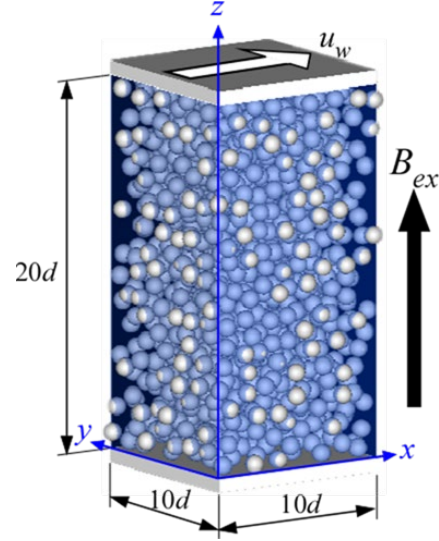


Fig. 1 Simulation model for magnetic particles in an MR fluid between two parallel plates.

3. Results and discussions

3.1 Particle structures and relative apparent viscosities

Figures 2(a) and 2(c) illustrate snapshots of the particle structures at steady state for various Mason numbers. Panel (a) shows a face-on view at $x = 10d$, and panel (c) shows a face-on view at $y = 0$. The color of each particle indicates the number of contacts with neighboring particles. Figures 2(b) and 2(d) depict the corresponding average particle volume fraction Ψ_p for panels (a) and (c), respectively. These values were obtained by integrating the particle volume fraction within the fluid computational lattice, Φ . In this study, hydrodynamic two-phase separation was observed under high shear rates: a particle-free region appeared near the moving wall, while an aggregate structure without interparticle contact formed near the stationary wall. For $Mn > 10$, particles moved away from the moving wall. At $Mn = 30$, the sheet-like structure fully collapsed, and a void region appeared near the moving wall. The particles became densely packed on the stationary wall side, but without direct physical contact, forming an aggregate structure. In this state, the particle volume fraction in the dense region (up to $z = 18.7d$) increased to 33 vol%. In contrast, at $Mn = 50$, corresponding to $R_H = 2.4$, the upper-layer particles of the aggregates detached and dispersed upward due to the high shear flow. At $Mn = 100$, the particles were further separated in both directions toward the moving and stationary walls, resulting in a dilute particle region at the center. The results for $Mn < 0.1$ (not shown here) show negligible differences compared to $Mn = 0.1$, as the dominant magnetic force maintains the chain-like structures. As the Mason number approaches $Mn \approx 1$, the magnetic and hydrodynamic forces reach a competitive regime, triggering a structural transition from chain-like to sheet-like structures.

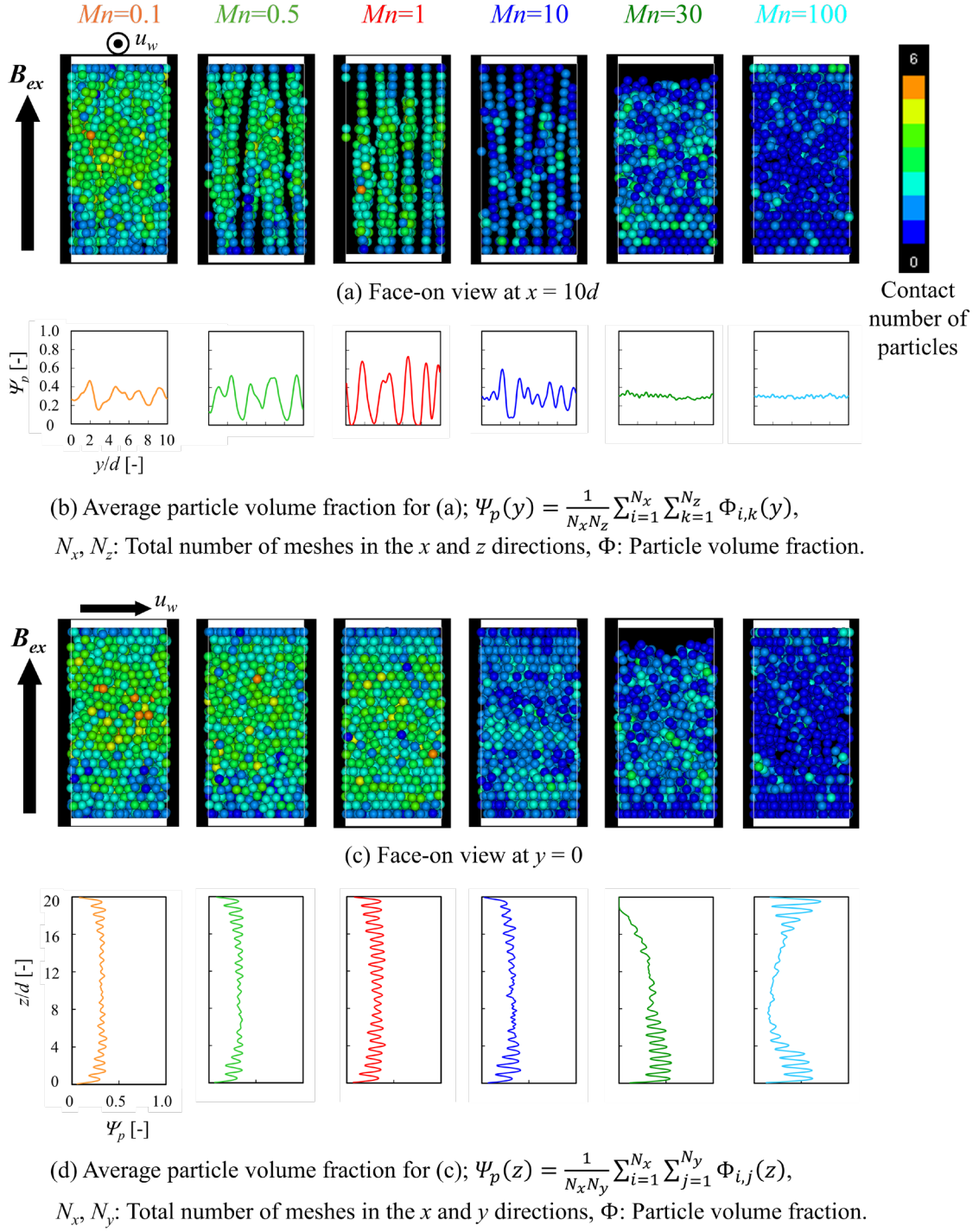


Fig. 2 Particle structure and average particle volume fraction at steady state for each Mason number.

Figure 3 depicts the relative apparent viscosity and the average particle contact number as a function of the Mason number. The average particle contact number $\langle N_c \rangle_T$ is defined as

$$\langle N_c \rangle_T = \frac{1}{T} \int_t^{t+T} \left(\frac{1}{N} \sum_{i=1}^N N_{c,i}(\tau) \right) d\tau, \quad (16)$$

where N is the total number of particles, $N_{c,i}(\tau)$ is the number of particles in contact with particle i at time τ , and T is

the averaging time in the steady state. The averages were calculated using $T \geq 50 \mu\text{s}$, and the averaging interval Δt was larger than the simulation time step $\Delta t = 15 \text{ ns}$. The error bars for the average contact number represent the sample standard deviations, which are small. In contrast, the error bars for the relative apparent viscosity are too small to be visible, indicating that the particle structure nearly reaches a steady state. Consistent with observations from previous experimental studies (Klingenberg et al., 2007; Berli and Vicente, 2012; Morillas and Vicente, 2020), the relative apparent viscosity in this study decreases exponentially until reaching a specific Mason number. The average particle contact number gradually reduces as the Mason number increases. However, for $Mn > 10$, the average contact number drops below 1. Figure 2 indicates that the microstructural visualizations reveal substantial structural differences for $Mn > 10$, even when the relative viscosities are similar. This indicates that the relationship between relative viscosity and particle structure is not strictly one-to-one.

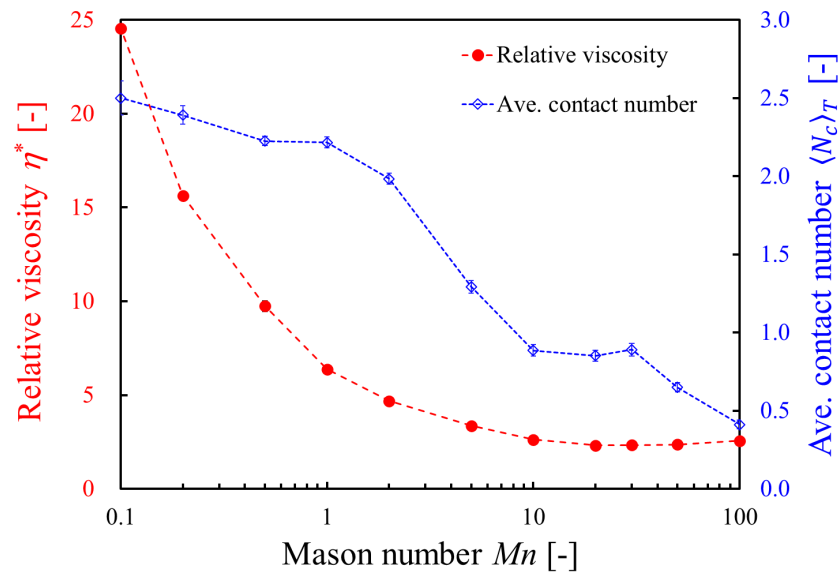


Fig. 3 Relative apparent viscosity and average contact numbers of particles as a function of Mason numbers.

In this study, the shear flow rate was varied while maintaining a constant value of $Mn \cdot R_H (= 120)$. As the shear flow rate increased under a constant magnetic field, the microstructures formed by the magnetic particles transitioned from chain-like to sheet-like and then to aggregate structures near the stationary wall. In addition, Fig. 1 indicates that since the external magnetic field is applied along the z -axis, the chain-like structure, with particles vertically aligned along the external magnetic field, is the most energetically stable. It is considered that the aggregation near the stationary wall at $Mn = 30$ results from a delicate balance between magnetic repulsive forces and hydrodynamic forces acting on the particles.

3.2 Tilt angle of particles

The histograms of the tilt angle of the magnetic moments of the particles relative to the external magnetic field are presented in Fig. 4, with an angle interval of 0.5° . As the Mason number increases, the peaks of $\Delta\theta$ distributions decrease, while the tilt angle and its distribution become larger and broader. For example, at $Mn = 1$ and 10 , the peaks of the tilt angle distribution occur at $\Delta\theta = 0.5^\circ$ and 3° , respectively. At $Mn = 30$, the peak shifts to 6.5° , with a tilt angle range from 2° to 13° . At $Mn = 50$, the peak moves further to 9.5° , with a broader range from 3.5° to 20.5° . At $Mn = 100$, the directions of the magnetic moments are widely distributed, and no distinct peak is observed. In this high-shear flow field, particles located near the moving wall are expected to gain a degree of rotational freedom and become dispersed. As a reference, the dashed lines in Fig. 4 represent the tilt angles calculated from the analytical solution for a single particle, $\Delta\theta = \sin^{-1}(\pi\eta d^3 \dot{\gamma} / 2\mu_0 m H_{ex})$, at each Mason number. Compared to the tilt angles obtained in the single-particle case, the peaks of the tilt angle distribution at low Mason numbers of $Mn = 1$ and 10 are slightly higher. This indicates that

hydrodynamic torque acts on the entire chain-like structure under these conditions. In contrast, at higher Mason numbers of $Mn = 30$ and 50 , the peaks decrease in magnitude. This outcome indicates that the hydrodynamic torque acting on individual particles is reduced due to the presence of densely packed neighboring particles arising from the two-phase separation.

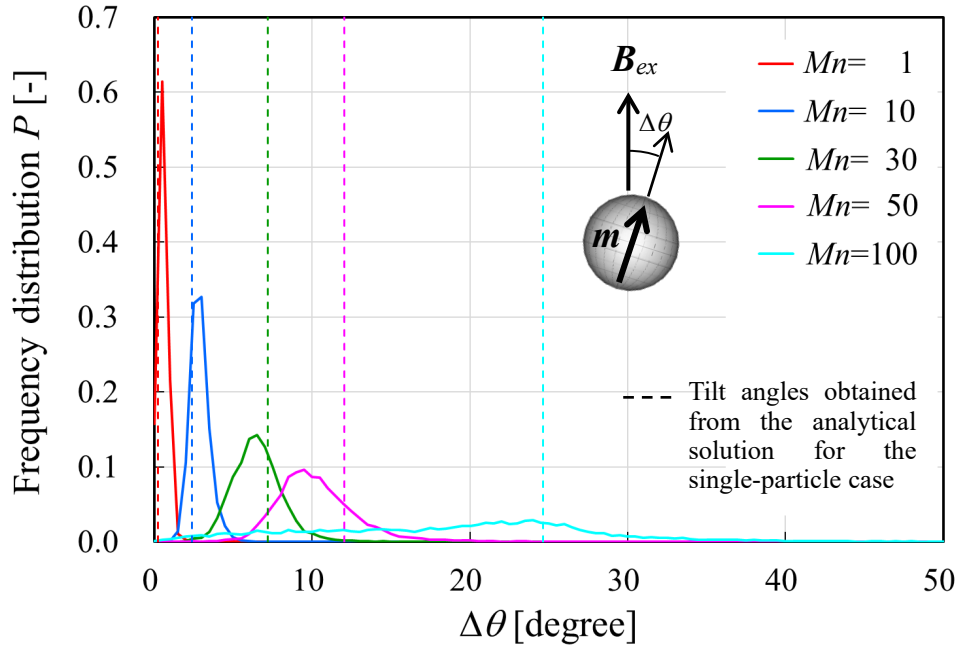
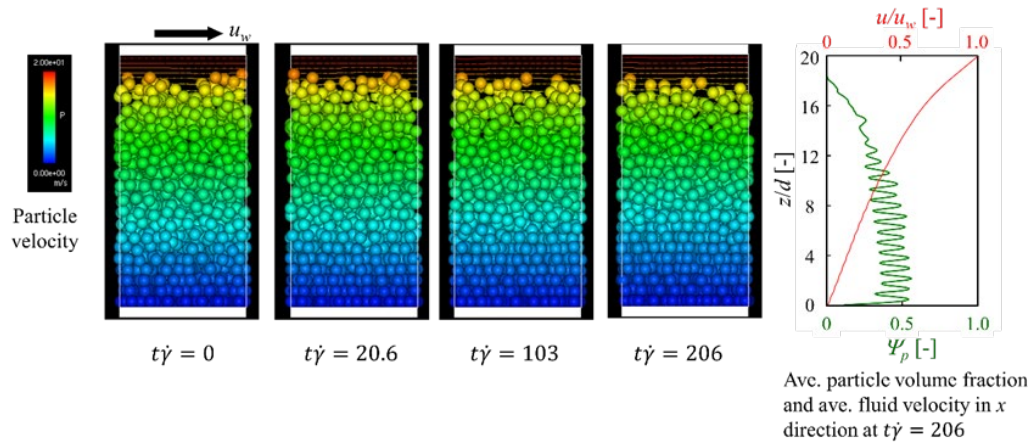


Fig. 4 Frequency distribution for tilt angle of particle magnetic moment on Mason numbers; Dashed lines indicate the tilt angles obtained from the analytical solution for the single-particle case at each Mason number: $\Delta\theta = \sin^{-1}(\pi\eta d^3\dot{\gamma}/2\mu_0 m H_{ex})$.

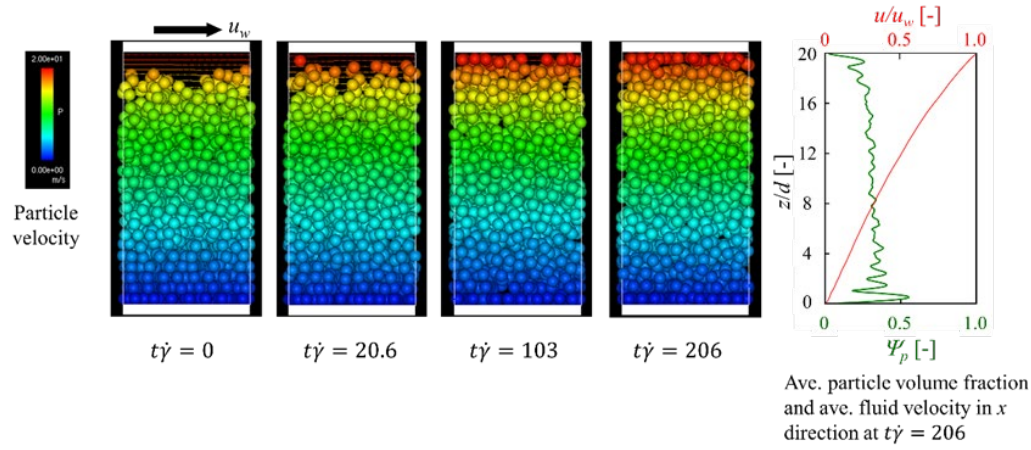
3.3 Effect of external magnetic field

Three simulations were performed to investigate whether the hydrodynamic lift force toward the stationary wall acts on particles whose rotation is constrained by an external magnetic field. Using the final state at $Mn = 30$ in Fig. 2 as the initial condition, simulations were conducted under the same shear flow condition as $Mn = 30$, both with and without magnetic interaction. Figure 5 provides snapshots of shear flow simulations of particles under both conditions. The graph on the right displays the average particle volume fraction and the average fluid velocity in the x direction at $t\dot{\gamma} = 206$. Figure 5(a) shows a continued simulation with magnetic interaction ($\mathbf{m} \neq \mathbf{0}$, $\mathbf{B}_{ex} \neq \mathbf{0}$), and Fig. 5(b) shows a virtual simulation without an applied magnetic field ($\mathbf{m} \neq \mathbf{0}$, $\mathbf{B}_{ex} = \mathbf{0}$), corresponding to $Mn = 30$ and $R_H \rightarrow 0$, and Fig. 5(c) shows a virtual simulation without magnetic interaction ($\mathbf{m} = \mathbf{0}$, $\mathbf{B}_{ex} = \mathbf{0}$), corresponding to $Mn \rightarrow \infty$ and $R_H \rightarrow 0$. The color of each particle indicates its velocity. Figure 5(a) shows that when shear flow is further applied, the particle structure is preserved, and a layered particle arrangement develops to some extent, accompanied by two-phase separation. In contrast, in Figs. 5(b) and 5(c), where particles are not rotationally constrained by the external magnetic field, the upper-layer particles in the aggregate structure are lifted toward the moving wall by $t\dot{\gamma} = 20.6$ and reach the moving wall at $t\dot{\gamma} = 103$. At $t\dot{\gamma} = 206$, the particles are dispersed across the region between the moving and stationary walls. In Fig. 5(b), the lift-induced aggregation structure collapses despite the presence of magnetic interactions among particles. These results indicate that rotational constraint by the magnetic field strongly influences the lift forces acting on particles, and that lift-induced aggregation toward the stationary wall can occur in mechanical devices employing MR fluids.

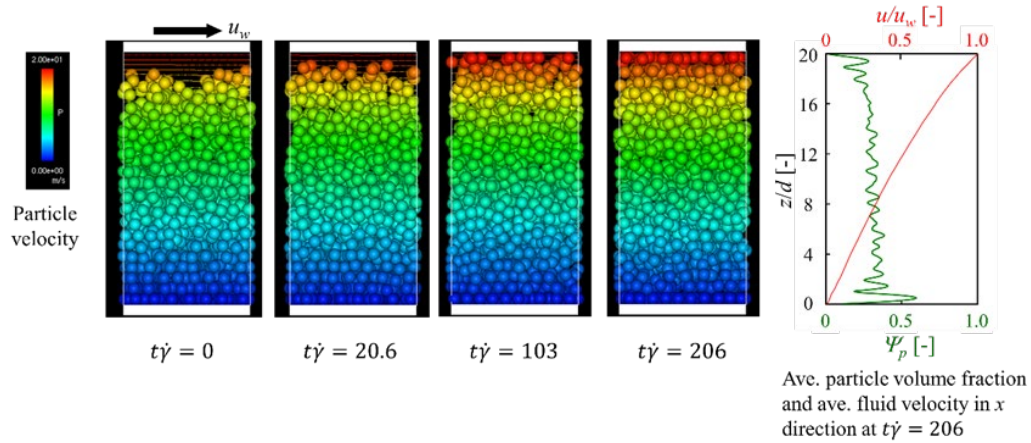
In this study, the angular momentum of the particles is zero because their rotation is constrained by the magnetic field. The lift force acting on the particles cannot be determined solely from magnetic torque and hydrodynamic torque; the velocity of the surrounding fluid must also be considered. In addition, the lift force can be either positive or negative depending on the relative rotational direction with respect to the surrounding fluid, making this phenomenon complex. Therefore, the lift force acting on particles at $Mn = 30$ is a subject for future investigation.



(a) $\mathbf{m} \neq \mathbf{0}$, $\mathbf{B}_{ex} \neq \mathbf{0}$ (Continuing calculation: $Mn = 30, R_H = 4$)



(b) $\mathbf{m} \neq \mathbf{0}$, $\mathbf{B}_{ex} = \mathbf{0}$ (Virtual calculation: $Mn = 30, R_H \rightarrow 0$)



(c) $\mathbf{m} = \mathbf{0}$, $\mathbf{B}_{ex} = \mathbf{0}$ (Virtual calculation: $Mn \rightarrow \infty, R_H \rightarrow 0$)

Fig. 5 Snapshots of shear flow simulations of particles with and without magnetic interactions, after the final state of $Mn = 30$ in Fig. 2; The contour lines in snapshots are streamlines. The graph on the right shows the average particle volume fraction and the average fluid velocity in the x direction at $t\dot{\gamma} = 206$.

4. Conclusion

In summary, the behavior of magnetic particles in a confined space was examined under constant magnetic interaction and particle volume fraction, assuming the upper limit of normal operation in practical MR fluid applications. The resulting microstructure formation was analyzed and correlated with relative apparent viscosity. At $Mn = 30$, hydrodynamic two-phase separation was observed with a void region near the moving wall. These results demonstrate that lift-induced aggregation toward the stationary wall can occur in devices using MR fluids and that there exists an upper shear flow rate limit for the stable operation of such devices. For instance, when MR fluid is used in brakes, it is essential to recognize that braking performance can deteriorate beyond a certain Mason number due to this hydrodynamic two-phase separation. For $Mn \geq 50$, the hydrodynamic force becomes dominant over the magnetic force, which previously constrained particle rotation, leading to the collapse of the particle structures. In the absence of a magnetic field ($Mn \rightarrow \infty$), where particle rotation is permitted, the shear-induced lift force acting on the particles is directed toward the moving wall. Based on the microstructures obtained in this study, the MR fluid under the condition $Mn \cdot R_H = 120$ appears to maintain the desired rheological properties down to approximately $Mn = 10$ (with $R_H = 12$). Thus, careful consideration of the $Mn \cdot R_H$ parameter is critical in the design of MR fluid devices. In this study, the $Mn \cdot R_H$ parameter was examined only under a single condition, $Mn \cdot R_H = 120$, as shown in Fig. 6. Classifying the particle structures formed on the Mn - R_H plane is a future challenge.

In addition, experimental observation of this phenomenon is required. The following challenges must be addressed to advance the practical application of MR fluids: the mechanism of lift force generation under particle rotational constraints, the construction of the Mn - R_H phase diagram, and the response speed required to restore the initial state after two-phase separation

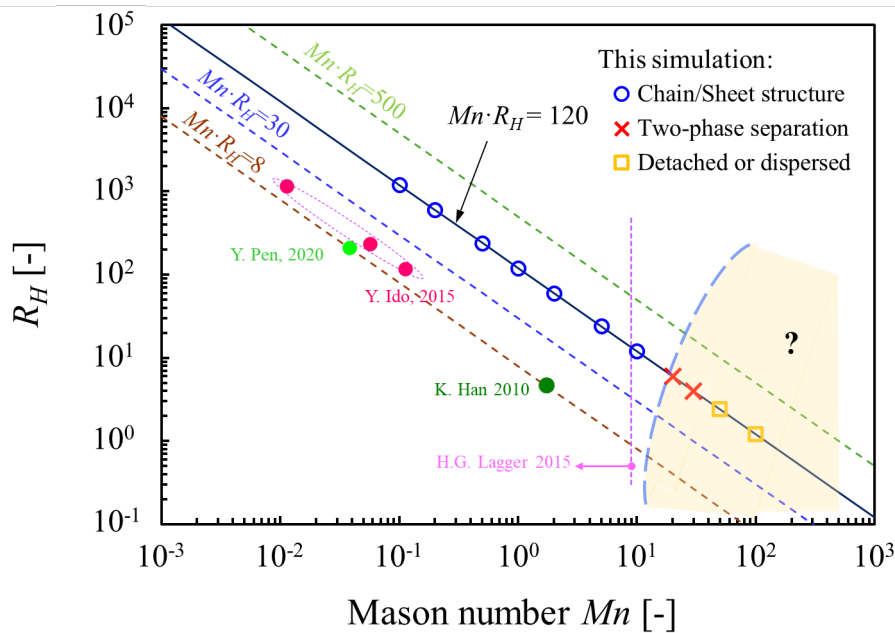


Fig. 6 Simulation results and references on the Mn - R_H plane.

Conflict of interest

The authors have no conflicts to disclose.

References

- Ando, T., Akamatsu, K., Nakao, S. and Fujita, M., Simulation of fouling and backwash in dead-end microfiltration: Effect of pore size, *J. Memb. Sci.*, Vol. 392-393 (2012), pp. 48-57.
- Ando, T., Katayama, D., Hirota, N., Koike, O., Tatsumi, R. and Yamato, M., Structure formation of magnetic particles under magnetic fields toward anisotropic materials, *IOP Conf. Series: Materials Sci. Engine.*, Vol. 424, No. 1 (2018), 012076, DOI:10.1088/1757-899X/424/1/012076.
- Berli, C. L. and de Vicente, J., A structural viscosity model for magnetorheology, *Appl. Phys. Lett.*, Vol. 101 (2012), 021903, DOI:10.1063/1.4734504.
- Blake, J. and Gurocak, H. B., Haptic glove with MR brakes for virtual reality, *IEEE/ASME Trans. Mechatronics*, Vol. 14, No. 5 (2009), pp. 606-615.
- Chikazumi, S., *Physics of Ferromagnetism*, 2nd ed (1997), p. 7, Oxford Science Publications.
- Fadlum, E. A., Verzicco, R., Orlandi, P. and Mohd-Yusof, J., Combined immersed-boundary finite-difference methods for three-dimensional complex flow simulations, *J. Comput. Phys.*, Vol. 161, No.1 (2000), pp. 35-60.
- Fujita, M. and Yamaguchi, Y., Simulation model of concentrated nanoparticulate flows, *Phys. Rev. E*, Vol. 77, No. 2 (2008), 026706, DOI: 10.1103/PhysRevE.77.026706.
- Han, K., Feng, Y. T. and Owen, D. R. J., Three-dimensional modelling and simulation of magnetorheological fluids, *Int. J. Numer. Meth. Engng.*, Vol. 84, No. 11 (2010), pp. 1273-1302.
- Ido, Y., Arakawa, K. and Sumiyoshi, H., Numerical simulation of behavior of magnetic particles in a simple shear flow, *J. Japanese AEM*, Vol. 23, No. 1 (2015), pp. 16-22 (in Japanese).
- Ido, Y., Sumiyoshi, H. and Tsutsumi, H., Simulations of behavior of magnetic particles in magnetic functional fluids using a hybrid method of lattice Boltzmann method, Immersed boundary method and discrete particle method, *Computers and fluids*, Vol. 142 (2017), pp. 86-95.
- Kajishima, T., Takiguchi, S., Hamasaki, H. and Miyake, Y., Turbulence structure of particle-laden flow in vertical plane channel due to vortex shedding, *JSME Int. J. Ser. B*, Vol. 44, No. 4 (2001), pp. 526-535.
- Klingenberg, D. J., Ulicny, J. C. and Golden, M. A., Mason numbers for magnetorheology, *J. Rheol.*, Vol. 51, No. 5 (2007), pp. 883-893.
- Kumar, J. S., Paul, P. S., Raghunathan, G. and Alex, D. G., A review of challenges and solutions in the preparation and use of magnetorheological fluids, *Int. J. Mech. Mater. Eng.*, Vol. 14, No. 1 (2019), 13, DOI:10.1186/s40712-019-0109-2.
- Lagger, H. G., Bierwisch, C. B., Korvink, J. G. and Moseler, M., Discrete element study of viscous flow in magnetorheological fluids, *Rheol. Acta.*, Vol. 53, No. 5 (2014), pp. 417-443.
- Lagger, H. G., Breinlinger, T., Korvink, J. G., Moseler, M., Renzo, A. D., Maio, F. D. and Bierwisch, C., Influence of hydrodynamic drag model on shear stress in the simulation of magnetorheological fluids, *J. Non-Newtonian Fluid Mech.*, Vol. 218 (2015), pp. 16-48.
- Li, W. H. and Du, H., Design and experimental evaluation of a magnetorheological brake, *Int. J. Adv. Manuf. Technol.*, Vol. 21, No. 7 (2003), pp. 508-515.
- Makabe, R., Akamatsu, K., Tatsumi, R., Koike, O. and Nakano, S., Numerical simulations of lift force and drag force on a particle in cross-flow microfiltration of colloidal suspensions to understand limiting flux, *J. Memb. Sci.*, Vol. 621 (2021), 118998, DOI:10.1016/j.memsci.2020.118998.
- Martin, J. E. and Anderson, R. A., Chain model of electrorheology, *J. Chem. Phys.*, Vol. 104, No. 12 (1996), pp. 4814-4827.
- Morillas, J. R. and de Vicente, J., Magnetorheology: a review, *Soft Matter*, Vol. 16, No. 42 (2020), pp. 9614-9642.
- Nakayama, Y. and Yamamoto, R., Simulation method to resolve hydrodynamic interactions in colloidal dispersion, *Phys. Rev. E*, Vol. 71, No.3 (2005), 036707, DOI: 10.1103/PhysRevE.71.036707.
- Nakayama, Y., Kim, K. and Yamamoto, R., Simulating (electro)hydrodynamic effects in colloidal dispersions: Smoothed

- profile method, *Eur. Phys. J. E*, Vol. 26, No. 4 (2008) pp.361-368.
- Pei, L., Ma, Z., Ma, D., Shi, X., Pan, H., Wang, P. and Gong, X., Simulations on the rheology of dry magneto-rheological fluid under various working modes, *Smart Mater. Struct.*, Vol. 31, No. 1 (2022), 015031, DOI:10.1088/1361-665X/ac36ad.
- Peng, Y. and Pei, P., Microstructure evolution based particle chain model for shear yield stress of magnetorheological fluids, *J. Intelligent Systems and Structures*, Vol. 32, No. 1 (2021), pp. 49-64.
- Rabinow, J., The magnetic fluid clutch, *AIEE Transactions*, Vol. 67, No. 2 (1948), pp. 1308-1315.
- Rosensweig, R. E., *Ferrohydrodynamics* (1985), pp. 15-16, 46-50, Cambridge University Press.
- Rossa, C., Jaegy, A., Lozasda, J. and Micaelli, A., Design considerations for magnetorheological brakes, *IEEE/ASME Tran. Mechatronics*, Vol. 19, No. 5 (2014), pp. 1669-1680.
- Sato, A., *Introduction to Molecular-Microsimulation of Colloidal Dispersions* (1995), pp. 185-186, Elsevier.
- Senkal, D. and Guricak, H., Spherical MR-brake with nintendo wii sensors for haptics, *Haptics: Generating and Perceiving Tangible Sensations: Int. Conf., Euro Haptics 2010, Proceedings Springer Berlin Heidelberg* (2010), pp. 160-165.
- Sherman, S. G., Becnel, A. C. and Wereley, N. M., Relating mason number to bingham number in magnetorheological fluids, *J. Magn. Magn.*, Vol. 380 (2015), pp. 98-104.
- Spencer Jr, B. F., Dyke, S. J., Sain, M. K. and Carlson, J. D., Phenomenological model for magnetorheological damper, *J. Eng. Mech.*, Vol. 123, No. 3 (1997), pp. 230-238.
- Tsuji, Y., Tanaka, T. and Ishida, T., Lagrangian numerical simulation of plug flow of cohesionless particles in a horizontal pipe, *Powder Technology*, Vol. 71, No. 3 (1992), pp. 239-250.
- Tsujita, T., Ohara, M., Sase, K., Konno, A., Nakayama, M., Abe, K. and Uchiyama, M., Development of a haptic interface using MR fluid for displaying cutting forces of soft tissues, In *2012 IEEE Int. Conf. Robotics and Automation*, IEEE, (2012), pp. 1044-1049.
- Yang, T. H., Son, H., Byeon, S., Gil, H., Hwang, I., Jo, G., Choi, S., Kin, S. Y. and Kim, J. R., Magnetorheological fluid haptic shoes for walking in VR, *IEEE Trans. Haptics*, Vol. 14, No. 1 (2021), pp. 83-94.